Methane steam reforming in water deficient conditions on Ir/Ce$_{0.9}$Gd$_{0.1}$O$_{2-x}$ catalyst: Metal-support interactions and catalytic activity enhancement

S.K. Cheah[a,b], L. Massin[a], M. Aouine[a], M.C. Steil[b], J. Fouletier[b,*], P. Gélin[a,*]

[a] *Univ Lyon, Université Claude Bernard Lyon 1, CNRS, IRCELYON, F-69626, Villeurbanne, France*
[b] *Univ. Grenoble Alpes, CNRS, Grenoble INP, LEPMI, 38000 Grenoble, France*[1]

ABSTRACT

This work reports on the study of steam reforming of methane under water deficient conditions over Ir/Ce$_{0.9}$Gd$_{0.1}$O$_{2-x}$ (Ir/CGO) catalyst with very low Ir loading (0.1 wt% Ir). The catalyst surface was studied before and after testing by X-ray photoelectron spectrometry (XPS) and aberration-corrected high-resolution transmission electron microscopy (HRTEM) with 1 Å best resolution. Ir/CGO was pretreated at 1173 K in He flow with less than 0.5 ppm O$_2$ prior to catalytic testing. This led to the formation of Ir metal nanoparticles (NPs) with narrow-size distribution (2.5–6 nm, mean size of 4 nm in diameter). Ir/CGO slowly activated during reaction until reaching a steady state with tenfold increase of CH$_4$ conversion rate. The initial catalytic activity was consistent with surface metal sites being the main active sites and the CGO support having no effect on the CH$_4$ conversion rate except the inhibiting influence on the thermodynamically favoured carbon accumulation. After completion of the activation during reaction, Ir was present in the form of metallic NPs with smaller mean size (ca. 1.7 nm) than before testing, and oxidized Ir in 3 + /4 + states. Metal support interactions were thought to be responsible for Ir oxidation and redispersion at the CGO surface during reaction. It is proposed that the improved catalytic activity is due to a synergy between highly dispersed Ir species and the CGO substrate through delocalization of the catalytic reactions in the vicinity of the Ir metal particles.

1. Introduction

Internal reforming is an attractive technology to be implemented in Solid Oxide Fuel Cells feed with natural gas or alternative hydrocarbon fuels, for extending their applicability. Direct Internal Reforming (DIR) is generally achieved using conventional Ni-cermets, which requires large excess of water vapour, including often oxygen and/or carbon dioxide, to avoid carbon deposition [1–4]. Moreover, owing to the endothermicity of the reforming process, a local cooling of the cell is observed inducing thermal gradient and mechanical stress that dramatically lowers the lifetime of the cells [5,6].

Various alternatives have been proposed to overcome these difficulties. A first way of research has been to propose anode components, which are less sensitive to carbon deposition than nickel, *i.e.*, ceria-containing anodes [7,8], ceria-doped catalysts [9–11], *etc.* Vernoux et al. [12] have proposed a new concept, *i.e.*, the Gradual Internal Reforming (GIR), in which the two anode functions *i.e.*, the steam reforming of the fuel and its electrochemical oxidation producing water vapour, are separated. The production of water vapour is used for the fuel reforming all along the anode channel. Consequently, only a small quantity of water vapour is required at the inlet of the cell. This concept has been experimentally demonstrated [13], and applied for other gases than methane [14–16]. More recently, using an original anode microstructure, state of the art anode materials, *i.e.* Ni-YSZ cermet, has been tested over 2000 h without noticeable deterioration of the performance of the cell feed with pure and dry hydrocarbons [17,18]. This feature was obtained, both by deposition of a catalytic layer onto the anode and by the design of an original current collector.

Proper GIR operation requires that the catalyst layer exhibits the following specific properties: (i) sufficiently high catalytic activity towards methane steam reforming (MSR), and (ii) high resistance against the thermodynamically favoured carbon formation due to high CH$_4$/H$_2$O (C/S) molar ratio at the anode (near to 10/1). In addition, decreasing operation temperatures of SOFCs (from 900 to 650 °C) is one of the main current objectives to improve the lifetime of the cells [19]. Ni is a commonly used MSR catalyst. It could meet the requirement (i). However, it prones to deactivate in water deficient conditions due to carbon formation [20,21]. Noble metals (Pt, Ru, Ir, Pd and Rh) are considered to be good substitutes for Ni: they are moderately active for steam reforming but highly resistant to carbon deposition [22]. These

metals are, obviously, expensive; however the metal loading is noticeably lower than 30–40 wt% typically used in Ni-YSZ cermets. Postole et al. [23] have given an overview of the literature data dealing with MSR on noble metal based catalysts. It should be pointed out that, in most of the studies, the noble metal loading was in the range 1–5 wt% and the C/S ratio was less than 1, which is not the GIR condition. It has also been shown that pure ceria and doped ceria are active for CH_4/H_2O reactions and particularly resistant to carbon formation under GIR conditions [10,24]. Even if these materials revealed a poor catalytic activity for methane reforming, they are interesting owing to this specific property.
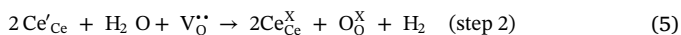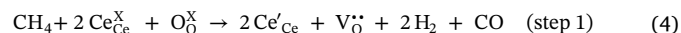
Interestingly, it has been shown that doping a Gd-doped ceria ($Ce_{0.9}Gd_{0.1}O_{2-x}$) by trace amount (0.1 wt%) of iridium (referred to as Ir/CGO) improves by more than two orders of magnitude the catalytic activity while maintaining the resistance to carbon formation under GIR conditions [11,18]. The improvement is not simply due to the Ir addition because it has been shown that the same amount of Ir supported on alumina catalyst does not induce the same activity [11]. This feature has also been pointed out by Gorte et al. with other noble metals as catalysts [25,26]. Consequently, the synergetic role of Ir catalyst and CGO support has been suggested [11]. However, since the Ir amount is very low and approaching the sensitivity limits of physicochemical characterization techniques, the mechanistic study on the catalytic process is difficult and the conclusions often speculative because the nature of the catalytic sites involved in the reaction steps of the mechanism are not known so far.

On the basis of thermodynamic calculations, it has been shown that, above 650 °C, the catalytic conversion of methane by water vapour is essentially governed by steam reforming, methane cracking, and water gas shift (WGS) reactions:

$$CH_4 + H_2O \rightarrow CO + 3H_2 \tag{1}$$

$$CH_4 \rightarrow C + 2H_2 \tag{2}$$

$$CO + H_2O \rightarrow CO_2 + H_2 \tag{3}$$

The water deficient conditions are thermodynamically favourable to carbon formation [21,27]. However, it has been shown that the nature of the catalytic layer has an important role on carbon deposition, which indicates that the reactions proceed via kinetic control over the catalyst and not by thermodynamic control. It is well admitted that Ni-YSZ cermets cannot be used as anodes in SOFCs fed with dry methane, owing to the high catalytic activity of nickel for carbon deposition. It has also been observed that carbon deposit does not form over ceria-based anodes [11,24,28].

It has been proposed that CGO catalyst activates methane with formation of reactive CH_x species, which reduce Ce(IV) to Ce(III) and produces CO and H_2 [10]. There has been a general agreement in the literature to conclude that the mechanism of CH_4/H_2O reaction over ceria based materials proceeds according to the following two steps, *i.e.*, a reduction of ceria by adsorbed molecules of methane, and a step involving H_2O inducing the re-oxidation of Ce^{3+} ions:

$$CH_4 + 2\,Ce_{Ce}^X + O_O^X \rightarrow 2\,Ce_{Ce}' + V_O^{\bullet\bullet} + 2H_2 + CO \quad \text{(step 1)} \tag{4}$$

$$2\,Ce_{Ce}' + H_2O + V_O^{\bullet\bullet} \rightarrow 2Ce_{Ce}^X + O_O^X + H_2 \quad \text{(step 2)} \tag{5}$$
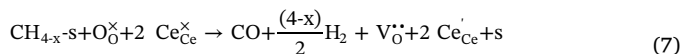
This mechanism is consistent with the first order rate of the H_2 production with respect to methane partial pressure [24,29]. The rate of methane reforming is controlled by the slow reaction of methane with oxygen on doped-ceria (step 1), and the rapid reaction between water vapour and reduced CGO (step 2) [24]. However, it has also been shown that doping CGO with Ir, even in a very small amount, increased considerably the rate of methane consumption with only small amounts of carbon deposit. Consequently, a three-step mechanism involving Ir sites and CGO surface sites has been suggested, using Kröger-Vink notation [30]:
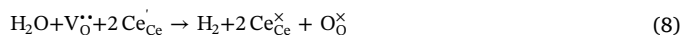
- the partial decomposition of CH_4 molecules over Ir sites (referred to as s) to form H_2 and CH_{4-x} species (step 1'):

$$CH_4 + s \rightarrow CH_{4-X}\text{-s} + \frac{X}{2}H_2 \tag{6}$$

- the reaction of CH_{4-x} species with reactive oxygen species on the CGO surface producing CO and H_2, with partial reduction of the ceria surface (step 2'):

$$CH_{4-x}\text{-s} + O_O^X + 2\,Ce_{Ce}^X \rightarrow CO + \frac{(4\text{-}x)}{2}H_2 + V_O^{\bullet\bullet} + 2\,Ce_{Ce}' + s \tag{7}$$

- a final step of regeneration of the oxygen ions of CGO lattice, involving H_2O (step 3'):

$$H_2O + V_O^{\bullet\bullet} + 2\,Ce_{Ce}' \rightarrow H_2 + 2\,Ce_{Ce}^X + O_O^X \tag{8}$$

In the absence of water vapour, the ceria substrate is progressively reduced by methane (steps 1' and 2'). Under GIR conditions with dry methane, the electrochemical oxidation of methane provides the water vapour needed for the substrate oxidation (step 3') avoiding the poisoning of the anode by graphitic carbon deposition.

In order to improve the performance of the catalyst, it is necessary to determine the nature of the active sites and to identify the parameters influencing their formation or degradation. It should be pointed out that the step 1' of the proposed mechanism, which involves surface Ir^0 sites, does not explain satisfactorily the high increase of the rate of methane conversion with addition of only trace amounts of noble metals on CGO support. Noble metal on alumina support does not perform equally well as the one with CGO support.

The present work consisted in (i) studying an Ir/CGO catalyst containing as low as 0.1 wt% Ir in the methane steam reforming reaction for potential use as anode material in SOFCs operated in GIR mode (water deficient conditions); (ii) obtaining experimental characterizations, which allow describing more precisely the active sites and explaining the catalytic behaviour. To this purpose, special care was paid to controlling the level of O_2 impurity present in the gases used for both activation and reaction in order to identify the key parameters influencing the activity. The samples were thoroughly analysed by XPS and ETEM before and after CH_4/H_2O reaction under water deficient conditions (GIR mode). The catalytic activity of the Ir/CGO catalyst was observed to be improved by one order of magnitude during one-day testing. Changes in the oxidation state and the dispersion of the iridium were clearly evidenced. The existence of metal support interactions between the noble metal and the CGO support was discussed to account for the strong improvement of the catalytic activity in methane steam reforming.

2. Experimental

2.1. Samples preparation

The powder sample was Ir/CGO (0.1 wt% Ir) prepared by impregnation of $Ce_{0.9}Gd_{0.1}O_{1.95}$ (CGO from Praxair, 43 $m^2\,g^{-1}$) with a solution of iridium acetylacetonate (Aldrich) in toluene. After complete evacuation of the solvent under reduced pressure, the catalyst was dried overnight at 393 K and calcined in flowing O_2 at 623 K for 6 h so as to obtain the so-called fresh Ir/CGO sample.

2.2. Physicochemical characterization

An FEI TITAN ETEM G2 80–300 kV instrument (0.085 nm resolution) equipped with an objective Cs aberration corrector was used for the observations of the catalyst. The microscope was also equipped with an energy dispersive X-ray (EDX) analyzer (SDD X-Max 80 m m^2 from Oxford Instruments) and a Gatan Imaging Filter Tridiem ERS (Gatan Instruments). The samples were crushed in ethanol and the solution was ultrasonically stirred before dropping it on a holey carbon-covered

copper TEM grid, followed by drying. Electron micrographs were analyzed using the ImageJ software to deduce a histogram of the Ir^0 particles size distribution.

The powder samples were investigated using X-ray photoelectron spectroscopy (XPS) and the analyses were carried out in a Kratos Ultra DLD spectrometer equipped with a hemispherical analyser and a delay line detector. All the data were acquired using monochromatic Al Kα radiation $E_{h\nu}$ (Al Kα) = 1486.6 eV (10 mA, 15 kV) as the photon source. The analyser was operated with a hybrid mode (combined electrostatic and magnetic lens) under ultra-high vacuum (5×10^{-9} Torr), a 160 eV pass energy for acquisition of survey and a 40 eV pass energy for acquisition of high-resolution core-level spectra of Ce4d, Gd4d, Ce3d, Ir4f, O1s, C1s. Charge neutralisation was used to compensate charges effects on samples and the area analysed was 700 μm x 300 μm.

All spectra were then calibrated using the Ce3d3/2 peak at 916.0 eV as the spectral reference. The latter corresponds to the principal Ce3d3/2 component of ceria (Ce^{4+}), and was chosen owing to its sharp, well-defined shape as well as to circumvent the uncertainty that often arises when the adventitious C1s contaminant peak is used as the reference instead. Quantification was carried out with the VISION software supplied. The relative sensitivity factors (RSF) applied here were inherent to this software and incorporate Wagner photoelectron cross-sections and analyser transmission correction.

Ir4f peaks were background-subtracted using a linear background. All other peaks were background-subtracted using a Shirley background. Curve-fitting was done with GL (30), which is a combination of Gaussian and Lorentzian (with 30 being the percentage of Lorentzian), or AS (60, 0.7) an asymmetrical peak shape, and with the relevant spin-orbit shifts and area ratios being applied. Ce3d peaks were curve-fitted, after subtracting a Shirley background, with Gaussian/Lorentzian product form GL (30) i.e. 30% of Lorentzian and the relevant spin-orbit shifts and area ratios being applied.

2.3. Catalytic testing experiments

The catalytic tests were carried out in a continuous flowing system at atmospheric pressure. The powder Ir/CGO sample (~ 5 mg) was placed in a tubular U-shaped quartz micro-reactor (Ø$_{internal}$ = 4 mm) and supported on a quartz wool plug. A thermocouple was placed in contact with the external wall of the reactor and close to the position of the sample in order to measure the temperature of the catalytic bed. Prior to the catalytic test, the sample was purged continuously with He (ultra-high purity grade, i.e., less than 0.5 ppm of H_2O and O_2) at a flow rate of 5.7 10^{-5} mol s^{-1} until complete air removal from the reactor (checked by mass spectrometry and micro gas chromatography). Afterwards, the sample was treated at 1173 K for 2 h (heating rate of 10 K min^{-1}). The catalytic reaction was performed at 923 K by introducing the reactants mixture which consisted of 4.76 mol% CH_4 and 1.03 mol% H_2O, and He as balance at a total molar flow rate of 8.08 10^{-5} mol s^{-1}. The Gas Hourly Space Velocity (GHSV) was ~ 67000 h^{-1}. Suitable water vapour concentration in the reaction mixture was obtained by flowing pure He through a saturator containing distilled water maintained at 290.7 K and mixed with 10 mol% CH_4 in He. The approach to equilibrium parameter of Steam Reforming and Water Gas Shift reaction could be determined by using the following equations:

$$\eta_{SR} = \frac{PH_2{}^3 PCO}{PCH_4\, PH_2O} \times \frac{1}{K_{eqSR}} \tag{9}$$

$$\eta_{WGS} = \frac{PH_2\, PCO_2}{PCO\, PH_2O} \times \frac{1}{K_{eqWGS}} \tag{10}$$

where K_{eqSR}, K_{eqWGS} are equilibrium constants of SR, and WGS respectively and Pj is the partial pressure of the species j (in atm). K_{eqSR} and K_{eqWGS} were 2.67 and 2.05 respectively, which were determined using the Gibb's free energies at 923 K.

An OmniStar^{TM} Pfeiffer Vacuum Quadrupole Mass Spectrometer (QMS) was used to analyse the effluent gases. Signals of H_2 ($m/z = 2$), CH_4 ($m/z = 15$), H_2O ($m/z = 18$), CO ($m/z = 28$), O_2 ($m/z = 32$), and CO_2 ($m/z = 44$) were continuously monitored. Calibrations of CH_4, O_2, CO_2, CO and H_2 were performed by using Messer certified mixtures of 1% CH_4/He, 1% O_2/He, 1% CO_2/He, 1% CO/He and 1% H_2/He mixtures before starting the experiments. H_2O was calibrated from the He flow saturated with H_2O vapour at 280.2 K. The signal at $m/z = 28$ was corrected for the contribution of the CO_2 fragmentation so as to obtain the CO concentration. For long duration monitoring of the catalytic reaction, CH_4, H_2 and CO_2 were analyzed with a Varian micro-GC equipped with appropriate columns (molecular sieve 5 Å and Porapak Q) and thermal conductivity detector (TCD).

The mass balance was determined for C, H and O elements at varying time on stream. The relative deviation between input and output (in %) for each element was calculated using the following equations:

$$\frac{([CH_4]_{in} F_{in} - [CH_4]_{out} F_{out} - [CO]_{out} F_{out} - [CO_2]_{out} F_{out})}{[CH_4]_{in} F_{in}} \times 100 \tag{11}$$

for C

$$\frac{\begin{aligned}(4 \times [CH_4]_{in} F_{in} + 2 \times [H_2O]_{in} F_{in} - 4 \times [CH_4]_{out} F_{out}\\ - 2 \times [H_2]_{out} F_{out} - 2 \times [H_2O]_{out} F_{out})\end{aligned}}{(4 \times [CH_4]_{in} + 2 \times [H_2O]_{in}) F_{in}} \times 100 \tag{12}$$

for H

$$\frac{([H_2O]_{in} F_{in} - [CO]_{out} F_{out} - 2 \times [CO_2]_{out} F_{out} - [H_2O]_{out} F_{out})}{[H_2O]_{in} F_{in}} \times 100 \tag{13}$$

for O, where "in" and "out" indexes stand for reactor inlet and outlet respectively, and F is the total molar flow rate.

The methane conversion rate expressed in mol s^{-1} g^{-1} was calculated according to the following equation:

$$CH_4\ conversion\ rate = \frac{[CH_4]_{in} F_{in} - [CH_4]_{out} F_{out}}{100 \times W} \tag{14}$$

where $[CH_4]_{in}$ and $[CH_4]_{out}$ are the CH_4 concentrations (in mol%), respectively, at the inlet and the outlet of the reactor, F_{in} and F_{out} the total molar dry flow rate (in mol s^{-1}) and W the weight of the Ir/CGO sample (g).

3. Results

3.1. Catalytic behaviour in CH_4/H_2O reaction at 923 K

Fig. 1 shows the variation of the mole fraction of the reaction products (H_2, CO and CO_2) with time on stream during catalytic conversion of 4.76 mol% CH_4/1.03 mol% H_2O (He balance, total flow rate of 8.08 10^{-5} mol s^{-1}) at 919 K over Ir/CGO (5.3 mg) pretreated in He at 1173 K. The temperature of the activation treatment was chosen according to the conditions required by the preparation of an electrochemical cell, especially to insure gas tightness and sealing operations [16]. Values of reactants and products mole fractions at three different times of the experiment are also reported in Table 1. The mole fractions of CO, CO_2 and H_2 released within the first 30 min of the reaction were low (resp. 0.03, 0.03 and 0.20 mol%) and even slightly decreased to reach minimum values of 0.02, 0.03, 0.14 mol% respectively after ca. 70 min. Afterwards, the mole fractions of formed CO, CO_2 and H_2 increased slowly up to maximum and stable values equal to 0.44, 0.12 and 1.74 mol%, respectively. It has to be noticed that stabilization of CO and H_2 production required much longer time on stream (ca. 25 h) than that of CO_2 formation (ca. 13 h).

Carbon, hydrogen and oxygen balance assessment is reported in Table 1. Carbon and hydrogen balances fit within less than 2%
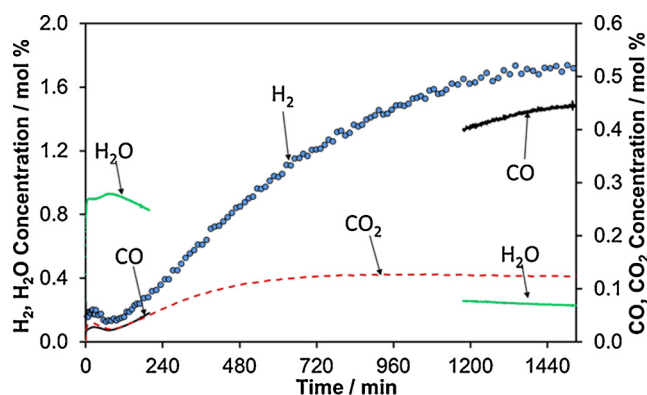
Fig. 1. Variation of H_2, CO, CO_2 and H_2O mole fractions with time on stream during CH_4/H_2O reaction on Ir/CGO at 923 K. The sample was pre-treated in He, at 1173 K, before testing. The CO and H_2O mole fractions were measured by QMS at the beginning (0–200 min) and the end of the experiment (beyond 1200 min).

Experimental conditions: 0.0053 g of Ir/CGO catalyst; 4.76 mol% CH_4/1.03 mol % H_2O, He balance; total flow rate of 8.08 10^{-5} mol s^{-1}.

deviation between the inlet and the outlet of the reactor, irrespective of the time on stream. The O balance would reveal increasing lack of O in products upon increasing time on stream, which is unlikely. This may rather be due to some experimental error on the measurement of the H_2O concentration by QMS. It should be mentioned that the H balance was much better than the O balance because the weight of CH_4 and H_2 concentrations (measured by GC with good accuracy) in the balance are much higher than that of H_2O concentration (measured by QMS with lower accuracy). From carbon balance results, it can be assessed that there was no accumulation of carbon during the test, which is in agreement with the reported high resistance of the Ir/CGO catalyst against carbon formation [30]. Observations of the sample by electron microscopy, shown in the next section, confirm the absence of any carbon deposits at the surface of CGO crystallites. Therefore, H_2, CO and CO_2 formations over Ir/CGO in a CH_4-rich CH_4/H_2O mixture can be explained by considering Steam Reforming (SR, reaction 1), responsible for CO formation, and Water Gas Shift (WGS, reaction 3), explaining CO_2 formation. The absence (or quasi-absence) of carbon deposits after testing contrasts with what is observed on Ni catalysts in these experimental conditions. This also supports the view that kinetics is fully controlling methane conversion since such highly deficient conditions have been shown to lead to extensive C deposition at the equilibrium on the basis of thermodynamic equilibrium calculations [18]. This is in agreement with values of the approach to equilibrium parameter for SR reaction (η_{SR}) lower than 0.9 10^{-4} (Table 1).

CH_4 conversion rates were calculated (Table 1) at three different times of the experiment. An increase from 6 10^{-6} mol s^{-1} g$_{cat}^{-1}$ to 7.2 10^{-5} mol s^{-1} g$_{cat}^{-1}$ was observed within 25 h reaction. The improvement of the CH_4 conversion rate by a factor of about 10 suggests the Ir/ CGO catalyst was deeply modified during the reaction. The slow kinetics of the process would be consistent with structural and/or chemical changes of the catalyst.

On the contrary to SR reaction, the equilibrium was reached for WGS reaction after 25 h on stream, indicating much higher rates than SR. Interestingly, the equilibrium was not reached at the beginning of the test (η_{WGS} = 0.1) and progressively increased up to 1. This would indicate that the WGS reaction is catalyzed by the Ir/CGO catalyst which activates during the run, finally leading to the thermodynamic control of the WGS reaction.

The experiment was repeated three times to check for reproducibility issues. Rates of CO, CO_2 and H_2 formation at steady state were reproducible within 17%, 4% and 10% error margin respectively. The Ir/CGO sample pretreated in high purity He (less than 0.5 vpm H_2O/O_2) at 1173 K always slowly activated during reaction, gaining between five and tenfold activity during the experiment. All experiments required overnight treatment in the reaction mixture at 923 K to reach the maximum activity. This suggests the occurrence of slow phenomena like atoms diffusion at the solid surface.

This activating behaviour was not observed in our previously reported experiments [11,30]. This could be due to the presence of O_2 at trace levels during the pretreatment step in our preceding experiments. The presence of as low as 10 ppm O_2 in the pretreament He gas is enough to change the Ir oxidation state and, as a consequence, the catalytic activity in CH_4/H_2O reactions [same authors, to be published].

XPS, HRTEM and STEM studies were performed to bring some insight into the possible changes responsible for the sharp activation of the catalyst and identify the active sites responsible for improved catalytic behaviour.

3.2. Electron microscopy studies

The Ir/CGO sample pre-treated in He, at 1173 K, was studied by aberration-corrected HRTEM and STEM before and after testing in $CH_4/$ H_2O mixture at 923 K. Fig. 2 shows a typical HRTEM image of the Ir/ CGO sample before testing (i.e. after treatment in He, at 1173 K). A nanoparticle sitting at the surface of CGO ($Ce_{0.9}Gd_{0.1}O_{1.95}$, JCPDS: 01- 075-0161) crystallizing in cubic structure with unit cell parameter equal to 5.418 Å can be clearly seen. The FFT pattern of the particle image (Fig. 2, inset) corresponds to a cubic structure with unit cell parameter equal to 3.8385 Å. It can be deduced that the observed nanoparticle is Ir metal (JCPDS: 03-065-9327). Two of the exposed planes are indexed in the image, indicating the Ir^0 particle is faceted. Using a smaller magnification (Fig. 3) allows concluding that Ir^0 particles are few in numbers at the surface of the CGO particles. STEM images (Fig. 4a and b) confirm TEM observations. A faceted Ir particle of about 4 nm in size can be seen in Fig. 4a while Fig. 4b shows the spatial distribution of Ir particles. It can be derived from TEM and STEM images that Ir particles have sizes in the range 2–6 nm with a mean size of 4.0 nm (Fig. 5).

Typical TEM and STEM images of the Ir/CGO sample after testing in CH_4/H_2O mixture at 923 K (catalytic data shown in Fig. 1) are given in Figs. 6 and 7 respectively. An iridium metal particle of ca. 1.5 nm can be seen in Fig. 6a, with (111) and (11$\bar{1}$) facets. The inset in Fig. 6a shows the FFT pattern indicating that the particle is metallic, as the one observed before testing. Fig. 6b shows another part of the sample observed with a lower magnification revealing 3 particles with about the
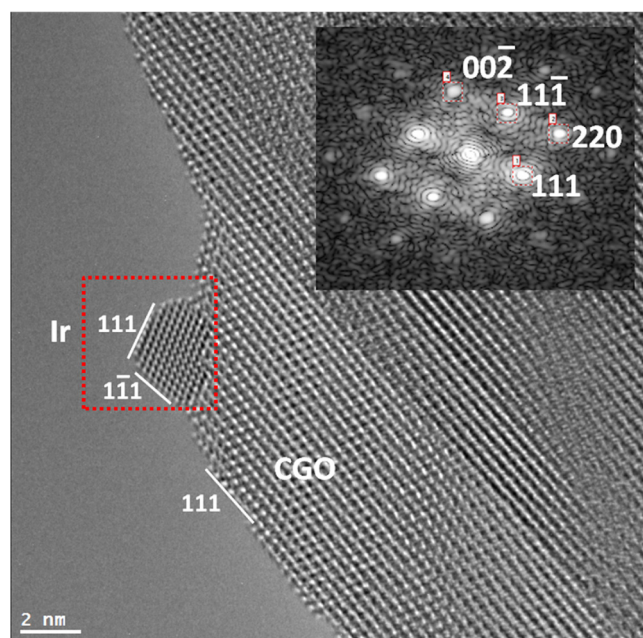
Table 1

Molar fractions of reactants and products at the reactor outlet, mass balance and CH_4 conversion rates obtained at varying times on stream (from Fig. 1). Experimental conditions are given in Fig. 1.

Time on stream (h)	Mole fraction (%)					Mass balance* (%)			CH_4 conversion rate (mol s^{-1} g$_{cat}^{-1}$)	Approach to equilibrium parameter	
	CH_4	H_2O	CO	CO_2	H_2	C	H	O		η_{SR}	η_{WGS}
0.25	4.70	0.90	0.03	0.03	0.18	0	0	3	6.14 10^{-6}	1.55 10^{-9}	0.10
3.2	4.69	0.83	0.05	0.05	0.28	−1	0	4	7.67 10^{-6}	1.06 10^{-8}	0.16
25.3	4.23	0.23	0.44	0.12	1.74	−2	0	10	7.18 10^{-5}	0.89 10^{-4}	1.01

* Definition is given in the experimental section.

Fig. 2. Aberration-corrected HRTEM image of the Ir-CGO sample before testing (Ir/CGO treated in He at 1173 K). Inset: FFT pattern of the particle image with indexed crystallographic planes corresponding to Ir metal.
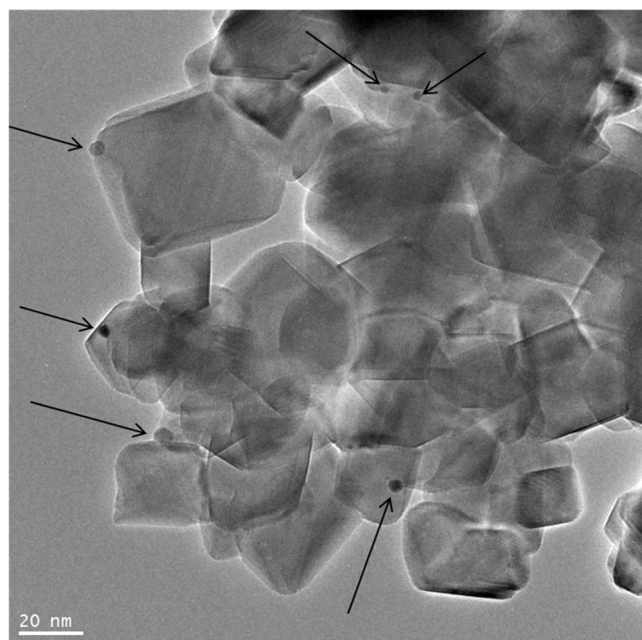

Fig. 3. TEM view of the Ir-CGO sample before testing (Ir/CGO treated in He at 1173 K). Ir particles are pointed out by arrows.

same size as in Fig. 6a (< 2 nm). Fig. 7a shows the STEM view of an Ir particle sitting at the CGO surface with the same size as in Fig. 6a while the STEM view with lower magnification (Fig. 7b) shows that particles are uniformly distributed on the CGO support and confirms the smaller size of the Ir particles after testing than before testing. The latter observation is clearly seen in the histogram (Fig. 5). Particles sizes are in the range 1.2–2.6 nm and the mean particle size equal to 1.7 nm. It can be then concluded unambiguously that the reaction mixture at 923 K induced the decrease of the iridium metal particles size. This is quite unexpected and this will be addressed in the discussion part. Interestingly, no carbon (graphite, amorphous carbon) could be detected by TEM.

3.3. XPS analysis

Since TEM/STEM studies cannot give alone unambiguous conclusions about the chemical state of the iridium in Ir/CGO before/after testing, XPS studies were performed.

Ir/CGO samples were analysed by XPS after calcination in O_2 at 623 K (fresh), after treatment in He at 1173 K before testing, and after subsequent testing in CH_4/H_2O at 923 K. The Ir4f spectra are shown in Fig. 8. All the binding energies are given in Table 2.

The XPS spectrum of the fresh sample (Fig. 8a) shows an asymmetric peak at high binding energy. The peak Ir4f7/2 is located at a binding energy of 61.5 eV, which corresponds to the energy of the oxidized iridium IrO_2 [31]. Such asymmetry is observed for the rutile-type IrO_2. It is also observed for amorphous iridium oxides (IrO_x) for which a mixture of Ir^{4+} and Ir^{3+} is detected and explains a larger peak width than for the rutile phase [31]. The binding energy of Ir^{3+} is found at 62.5 eV, which is different from most of the XPS results for oxides. In our case, considering the small amount of iridium present in the catalyst, it is difficult to assess that if the detected oxide contains only pure Ir^{4+} or if it contains also a small amount of Ir^{3+}, which the binding energy in the literature is reported at 62.3/62.7 eV [32]. At 623 K, the reactivity between IrO_x and CGO appears unlikely, which thus excludes the migration of iridium oxide within the ceria bulk. It can be concluded that all the iridium contained in the fresh Ir/CGO sample (after calcination in O_2 at 623 K) was probed by XPS. The binding energy of the peak Ir4f7/2 found at 61.5 eV corresponds to the energy reported in literature [31] for unsupported powders, so it would be assumed that the support has no effect on the iridium oxide particles of the fresh Ir/CGO sample.

Fig. 8b displays the spectrum corresponding to the catalyst after treatment in He, at 1173 K. The binding energy of the Ir4f7/2 peak, equal to 60.3 eV, is close to the energies reported for metallic iridium, *i.e.*, around 60.8 eV. Therefore, the thermal treatment in He appears to induce a reduction of the iridium oxide particles. The shift of -0.5 eV in binding energy can be explained by a Surface Core Level Shift (SCLS). In fact, surface atoms have an electronic structure different from bulk atoms, which results in a difference in valence bandwidth. This difference in bandwidth induces a shift of the valence band of the surface atoms and, consequently, a shift of the core levels [33]. Bianchi et al. have measured a shift of −0.55 eV for iridium atoms located in a (111) single crystal surface [34]. This experimentally measured shift is in agreement with that found for metal iridium particles of Ir/CGO whose size, measured by TEM, was of the order of 4 nm. Indeed, for such particles, the proportion of surface atoms is high enough to give a significant contribution to the XPS spectrum. It should be also noticed that no SCLS was observed when iridium is oxidized [32]. The reduction of IrO_x to Ir metal after treatment under He at 1173 K is consistent with thermodynamical data because at this temperature, IrO_2 dissociate to $Ir + O_2$ when the oxygen pressure is lower than 3.04 kPa [35]. Therefore, in the case here, at 1173 K, and with PO_2 of less than 0.05 Pa, IrO_2 dissociated to metallic Ir.

Fig. 8c displays the Ir4f spectrum of the Ir/CGO sample after reaction in CH_4/H_2O mixture at 923 K. Both Ir4f7/2 and Ir4f5/2 signals are broader than those corresponding to the sample treated in He at 1173 K and also present an asymmetry towards the higher binding energies. The decomposition of the peak gives two components at 60.7 eV and 61.5 eV. The component at 60.7 eV can be attributed to metallic iridium. It is shifted by + 0.4 eV with respect to the peak observed for metallic iridium in the sample treated in He at 1173 K. From TEM and STEM observations, Ir particles of smaller sizes (ca. 2 nm) than before testing (ca. 4 nm) are present. Since, for such small particles, the SCLS effect previously described must be considered, it appears that an additional effect should compensate the SCLS effect and even cancel it by inducing a shift of same magnitude and opposite sign [36]. It is well known that such small particles may have lost their metallic properties and exhibit an insulating character. In this case, the so-called metal/
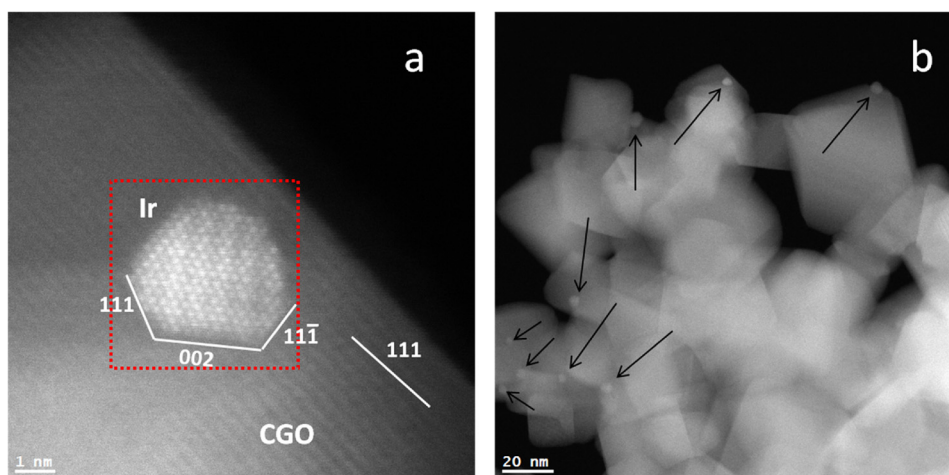
Fig. 4. STEM images of the Ir-CGO sample before testing (Ir/CGO treated in He at 1173 K). (a) observation of a faceted nanoparticle of iridium; iridium atoms appear as bright dots; (b) low magnification view; iridium particles are pointed out by arrows.
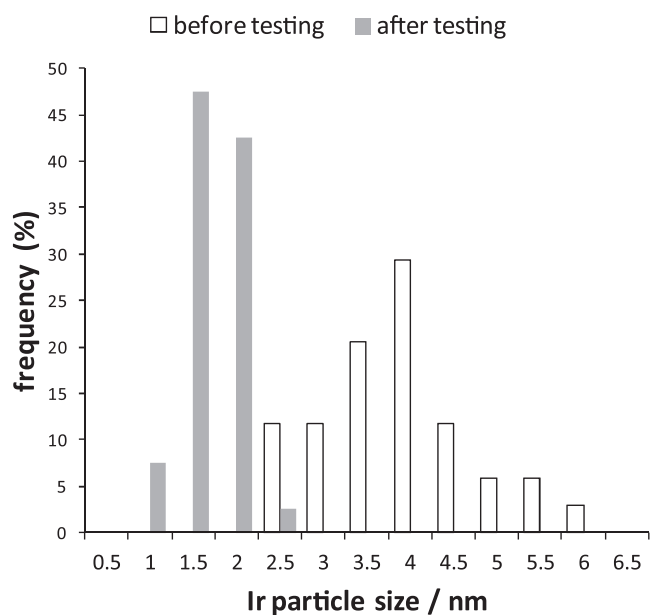

Fig. 5. Histogram of the Ir particles size distribution in Ir/CGO before and after testing.

insulator transition induces a final state effect which influences the XPS measurement. This effect arises from the fact that the photoelectron extracted during the measurement leaves a hole which is no longer filled by a neighbouring electron. The residual hole induces, by dipolar effect, a positive shift of the measured binding energy [33]. The peak at 61.5 eV would correspond, as proposed above, to Ir^{4+} or Ir^{4+}/Ir^{3+}, resulting from partial reoxidation of metallic Ir species.

In XPS studies, the quantification of the atomic ratio of two elements requires the use of the photoionization cross-section of electronic levels, the inelastic electron mean free path and the transmission energy function of the spectrometer. Since the inelastic electron mean free path and the transmission function both depend on kinetic energy, it is useful, to facilitate the quantification, to use core levels very close in energy such as Ce 4d and Gd 4d levels. In Table 3, the Gd atomic fraction defined as $[Gd]/([Gd] + [Ce])$ for varying samples was calculated using high-resolution Ce 4d and Gd 4d spectra. As an example, Fig. 9 shows the Ce 4d and Gd 4d spectra of the Ir/CGO sample after reaction in CH_4/H_2O mixture at 923 K.

The values of $[Gd]/([Gd] + [Ce])$ for all samples vary in the range 0.16–0.20. This variation is not significant owing to uncertainties on the Gd 4d baseline. The average value of $[Gd]/([Gd] + [Ce])$, equal to 0.18 (+/− 0.02), reliably exceeds that derived from chemical analysis, equal to 0.11. This result shows, therefore, a Gd enrichment at the CGO surface in agreement with literature [37,38].
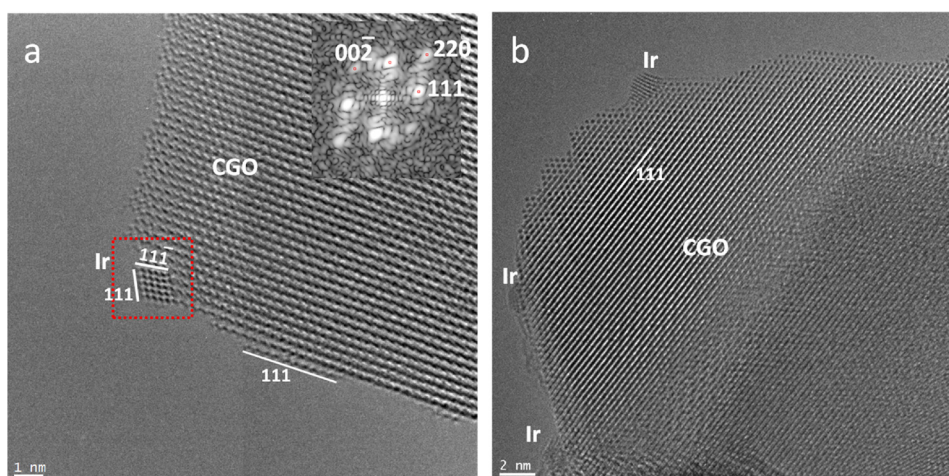

Fig. 6. TEM images of the Ir-CGO sample after testing in 5% CH_4/1% H_2O mixture, at 923 K (experiment described in Fig. 1). (a) aberration corrected HRTEM image showing a 1 nm Ir metal particle; inset: FFT pattern of the particle; (b) view of two Ir particles sitting at the surface of the CGO crystallites.
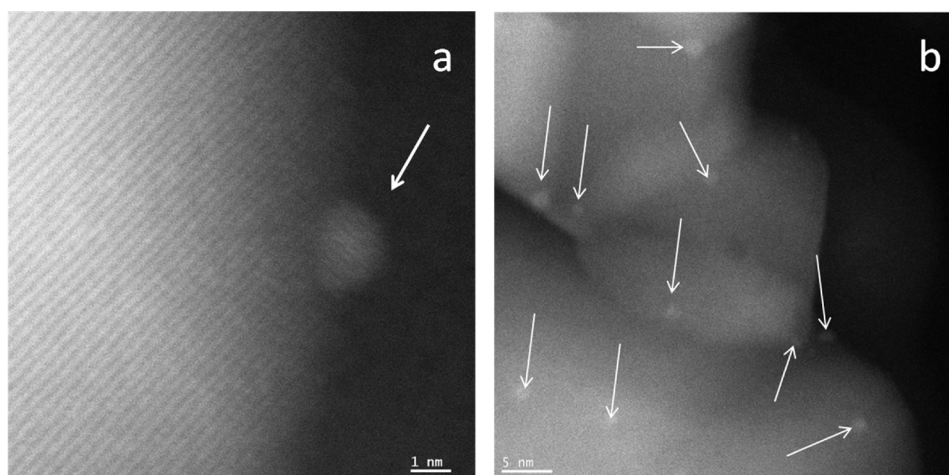
Fig. 7. STEM images of the Ir-CGO sample after testing in 5% CH_4/1% H_2O mixture, at 923 K (experiment described in Fig. 1). (a) view of an Ir nanoparticle; (b) view of several Ir particles by using lower magnification; particles are pointed out by arrows.

The atomic [Ir]/([Ce] + [Gd]) ratio was determined from Ir 4f, Ce 4d and Gd 4d for all Ir/CGO samples and reported in Table 3. [Ir]/ ([Ce] + [Gd]) varies between 0.0019 and 0.0022, which indicates that it is almost the same regardless of the treatment. It can be derived that the whole amount of iridium deposited by impregnation was analyzed by the XPS measurements, irrespective of the treatment, thus suggesting no migration of Ir species within the CGO bulk or loss of Ir in the gas phase by formation of volatile species.

XPS Ce 3d spectra were used to determine the relative amount of Ce in the + 3 oxidation state for various samples. The Ce 3d core level region and fitted results for the used Ir/CGO sample are shown in Fig. 10, as an example. The Ce 3d spectra are decomposed into ten components using the notation found in the literature [39]. Accordingly, v_0, v', u_0, and u' reflect Ce^{3+} ions while the other peaks are due to Ce^{4+} ions. The relative amount of Ce in the 3+ oxidation state is calculated according to the formula:

$$\frac{[Ce^{3+}]}{[Ce^{3+}] + [Ce^{4+}]} = \frac{area(v_0, \ v', \ u_0, \ u')}{total \ area} \quad (15)$$

Quantitative data for all samples are reported in Table 4. Due to the complexity of the Ce 3d spectrum decomposition, the absolute values of the Ce^{3+} atomic fraction in various samples are determined with an error. However, the use of the same fitting procedure for all samples should limit the relative error so that a variation as low as 0.05 on the atomic fraction value could be considered as relevant, thus allowing the results to be compared to each other and a general trend to be derived. The same method of Ce3d spectrum decomposition was already successfully applied to doped ceria samples and it was shown that the dopant could influence the $[Ce^{3+}]/([Ce^{3+}] + [Ce^{4+}])$ ratio [40]. By comparing fresh Ir/CGO and Ir/CGO treated in He at 1173 K, a decrease of the Ce^{3+} atomic fraction from 0.27 to 0.20 was observed. This decrease can be clearly visualized in Fig. 11 with the appearance of a shoulder at ca. 884 eV after normalizing the signals with respect to the v component. This could be explained by the iridium reduction, and an oxygen transfer to ceria *i.e.* oxidation of Ce^{3+} into Ce^{4+}. However, the same tendency was observed without iridium, making this hypothesis unlikely. The observed decrease of the surface Ce^{3+} species concentration upon thermal treatment at 1173 K could then be preferably related to sintering. The surface area decreased from 47 to 10 m^2/g upon treatment of CGO at 1173 K and TEM observations confirm the growth of CGO particles upon heating at 1173 K in He. It was observed recently that size increase of ceria nanoparticles from 4 to 120 nm could lead to decreasing the concentration of the surface oxygen vacancies [41]. Sintering could also influence the exposed crystal planes of ceria which were recently shown to be determinant on the concentration of

surface defect sites (oxygen vacancies) [42].

Upon reaction in CH_4/H_2O mixture at 923 K, the Ce^{3+} atomic fraction in Ir/CGO is shown to increase to 0.25, which indicates the reduction of some Ce^{4+} into Ce^{3+}. This could be explained by the strongly reductive character of the used atmosphere (5 times more CH_4 than H_2O). A reaction mixture containing 50% CH_4 and 5% H_2O in N_2 at 1173 K over the same CGO sample was shown to reduce 2% of the Ce in the CGO lattice from Ce^{4+} to Ce^{3+} [11]. It is concluded that both sintering and reductive atmospheres induce some $Ce^{4+} \rightarrow Ce^{3+}$ reduction in CGO but the phenomenon is not dependent on the presence of Ir.

4. Discussion

On the basis of XPS analysis, there is clear evidence that, before catalytic testing and upon activation in He at 1173 K, Ir in the Ir/CGO catalyst is exclusively at the metallic state. This is confirmed by TEM micrographs and FFT treatment of the images demonstrating the presence of metal particles deposited on the CGO support. Based upon the mean Ir particle diameter deduced from TEM data (Fig. 5), Ir dispersion equal to 0.27 could be derived from the formula:

$$Ir \ dispersion \ = \ \frac{1.1}{Ir \ nanoparticles \ size \ in \ nm} \quad (16)$$

[43,44]

Turn over frequency of methane conversion could be then calculated at the beginning of the test run according to the formula:

$$TOF \ = \ \frac{CH_4 \ conversion \ rate \ (mol \ s^{-1} g^{-1})}{Total \ amount \ of \ Ir \ (mol \ g^{-1}) \ \times \ Ir \ dispersion} \quad (17)$$

A value of 4.4 s^{-1} was obtained (reaction conditions: T = 923 K, 5 mol% CH_4 /1 mol% H_2O, He balance, 1 atm). In their study of Ir catalysts supported on ZrO_2 and γ-Al_2O_3 in CH_4/H_2O reaction, Wei and Iglesia reported forward CH_4 turnover rates varying from ca. 8 to ca. 19 s^{-1} upon dispersion varying from 0.25 up to 0.65 (T = 873 K, 20 mol% CH_4, 25 mol% H_2O, Ar balance) [45,46]. Comparing our results with literature requires calculations and assumptions. Assuming the reaction is of first order with respect to CH_4 and insensitive to H_2O concentration [45,46] and using the reported value of 87 kJ mol^{-1}, forward turnover rates reported by Wei and Iglesia [29] could be recalculated for the experimental conditions used in the present study: 4 s^{-1} for the reported dispersion of 0.25 (measured by H_2 chemisorption assuming 1:1 H:Ir stoichiometry). This value is close to the one obtained in the present study at the beginning of the test run, suggesting no difference of catalytic behaviour of Ir metal particles in CH_4/
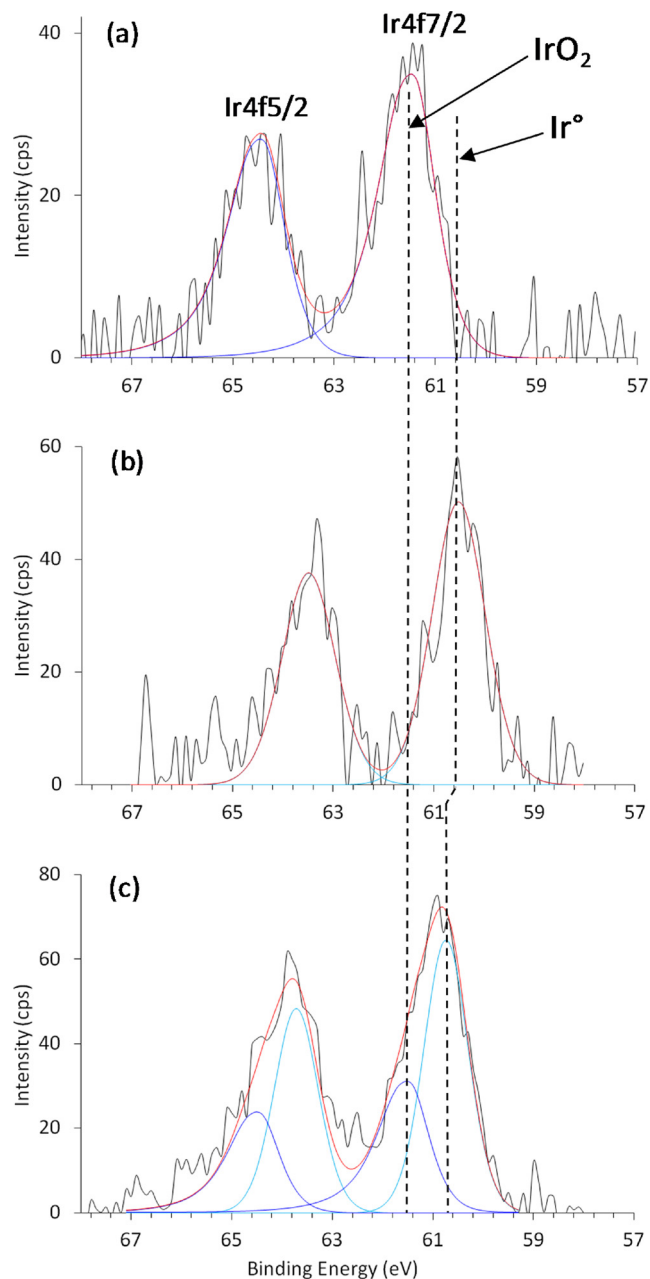
Fig. 8. Ir 4f XPS spectra of Ir/CGO samples: (a) fresh, (b) treated in He at 1173 K (before testing), (c) after testing in CH_4/H_2O at 923 K.

Table 2

: Binding energy of Ir4f7/2 determined by XPS after curve-fitting.

Sample	Binding energy (eV)		
Ir CGO fresh	–	–	61.5 (1)
Ir CGO treated in He at 1173 K (before testing)	60.3 (1)	–	–
Ir CGO after testing in CH_4/H_2O at 923 K	–	60.7 (0.6)	61.5 (0.4)

Values in parentheses correspond to the atomic fraction of Ir in the corresponding state.

H_2O when using non reducible oxides (ZrO_2, Al_2O_3) and a reducible one (CGO) as supports.

It has to be pointed out that SR reaction is usually performed in an excess of H_2O to prevent carbon deposition by methane cracking and deactivation by C poisoning of surface active sites (*e.g.* [29]). The fact

Table 3

[Gd]/([Gd] + [Ce]) and [Ir]/([Ce] + [Gd]) atomic ratios in various samples determined by XPS.

Sample	[Gd]/([Gd] + [Ce])[*]	[Ir]/([Ce] + [Gd])[*]
CGO, untreated	0.186	–
CGO, treated in He at 1173 K	0.166	–
Ir/CGO, fresh	0.161	0.0019
Ir/CGO, treated in He at 1173 K (before testing)	0.196	0.0022
Ir/CGO, after testing in CH_4/H_2O at 923 K	0.205	0.0022

[*] Ir 4f, Ce 4d and Gd 4d core levels are used.
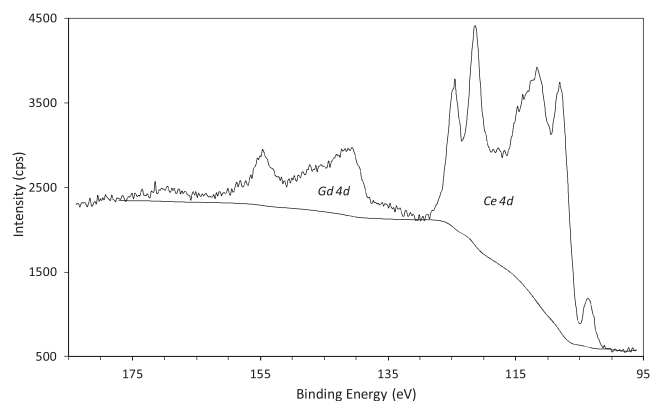

Fig. 9. Ce 4d and Gd 4d XPS spectra of the Ir/CGO sample after testing in CH_4/H_2O at 923 K.
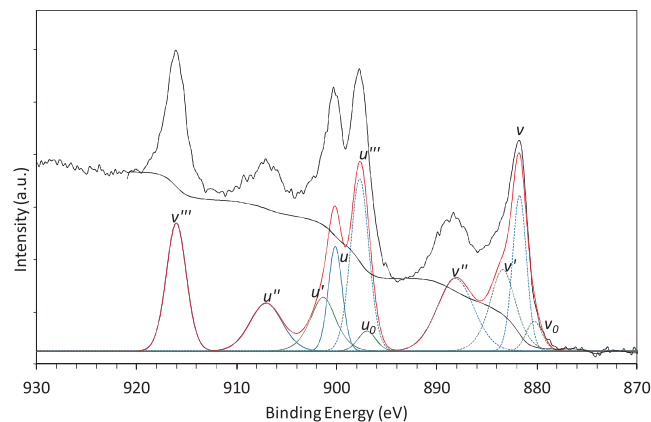

Fig. 10. XPS Ce 3d spectrum of the used Ir/CGO sample. Upper part: experimental data with the Shirley background; lower part: curve fitting after background subtraction.

Table 4

Atomic fractions of cerium ions in the +3 oxidation state for CGO and Ir/CGO samples after various treatments.

Sample	$[Ce^{3+}]/([Ce^{3+}] + [Ce^{4+}])$
CGO untreated	0.29
CGO treated in He at 1173 K	0.20
Ir CGO fresh	0.27
Ir CGO treated in He at 1173 K (before testing)	0.20
Ir CGO after testing in CH_4/H_2O at 923 K	0.25

that the Ir/CGO catalyst exhibits the same activity in water deficient conditions as Ir/ZrO_2 in CH_4 deficient conditions could then be due to the specific ability of the CGO support to prevent the poisoning of the active phase by carbon and then maintain the activity at constant level.
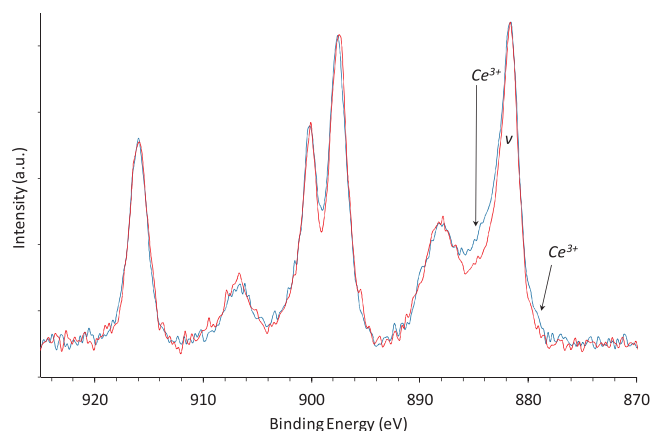
Fig. 11. XPS Ce 3d spectra of fresh Ir CGO (blue), and Ir CGO treated in He at 1173 K (red) after Shirley background subtraction. The signals were normalized with respect to the v component (For interpretation of the references to colour in this figure legend, the reader is referred to the web version of this article).

The high resistance of Ir/CGO was previously demonstrated by temperature programmed reduction experiments in CH_4 (TPR-CH_4) showing the progressive reduction of the CGO support with CO and H_2 formation without any C deposition until complete disappearance of reducible oxygen species in CGO [11,30]. By contrast, TPR-CH_4 experiment on Ir/Al_2O_3 was shown to lead to extensive C deposition accumulating on the catalyst [11]. The CGO support may then play a role in preventing C poisoning of the Ir surface. This is confirmed by the TEM data of the present study showing that no (or little) carbon formed during the reaction over Ir/CGO in water deficient conditions.

The striking feature from our present catalytic data is the slow activation of the Ir/CGO catalyst during the reaction, leading to the improvement of its activity by as much as one order of magnitude. The time required by the process (more than 1 day) is consistent with structural/chemical changes in the solid, finally affecting catalytic activity. Two main observations can be made for the Ir/CGO catalyst after testing: the mean metal particles size has decreased from 4 nm mean diameter to 1.7 nm and 40% of the Ir was oxidized during the reaction.

The tenfold increase of the specific rate of CH_4 conversion during the test run could thus be explained in two ways: (i) the structure sensitivity of the SR reaction over supported metal catalysts, *i.e.* the effect of the particle size on the catalytic properties; (ii) the formation of catalytic sites being more active than Ir metal particles and related to the oxidation of the Ir metal particles in the reaction mixture.

Theoretical studies do show that for methane the activation energy of the forward dissociation reaction on metal surfaces is strongly structure sensitive, low coordination sites being more active in CH_4 activation than exposed planes [47]. It is well established that over supported metal catalysts, the rate determining step of the MSR reaction is the methane activation, *i.e.* the C–H bond breaking. Experimental data reported by Wei et al. for CH_4/H_2O reactions over Ir catalysts supported on Al_2O_3 and ZrO_2 were in agreement with theoretical findings [46]. But contradictory experimental results were also reported [48]. Participation of very active species could not be totally ruled out by Wei et al. to explain the improved performance of their highly dispersed samples [46]. It has to be pointed out that the catalytic improvement by 2.3 measured upon increasing dispersion from 0.3 up to 0.7 was much lower than the tenfold improvement of the rate measured in the present work for similar variation of mean Ir particle size.

Electronic interactions between metal nanoparticles and oxide supports like ceria were also proposed to control stability, activity and selectivity of catalysts [49]. Electron transfer from the metal to the support was measured for well-defined Pt/ceria catalysts by combining synchrotron-radiation photoelectron spectroscopy, scanning tunnelling microscopy and density functional calculations [50]. It was found that

the charge transfer increased with the particle size, reaching a maximum at particle sizes around 50 atoms. It seems therefore that this effect mostly occurs for metal particles below 1.5 nm in size. In the present study the mean size of the Ir particles was higher than 1.7 nm, which seems to exclude this phenomenon as being the main cause of the observed catalytic enhancement. Although particle size effects can partly explain the catalytic activity improvement of the Ir/CGO catalyst during reaction, we suggest that additional effects have to be considered.

In recent studies, single metal atoms anchored to oxide supports such as ceria were proposed as catalytic sites [51]. Such sites may be more active in catalytic reactions than metal surfaces. Spin-polarized DFT + U approach was recently used to investigate the dissociative adsorption of methane on Ni deposited on stoichiometric and reduced cerium oxide surfaces in comparison with the extended Ni(111) surface. Supported Ni^{2+} and Ni° atoms were shown to have an effective CH_4 dissociation barrier that is about 40% and 80% smaller than that for Ni (111), respectively [52]. Using DFT calculations a ceria "nanopocket" was identified at the ceria surface with the property of binding Pt^{2+} so strongly that it could withstand sintering and bulk diffusion. Such sites were potentially active for fuel cell applications [53]. In the present work, we have no experimental evidence for the existence of such sites on Ir/CGO after testing.

Therefore we propose a model according to which the catalytic sites responsible for the catalytic activity after activation in the reaction mixture would involve not only surface sites of small Ir metal nanoparticles but also the interface between these particles and the CGO support.

The model was previously developed for oxygen reduction on a microelectrode on a solid oxide electrolyte that constitutes a Triple-Phase Boundary (TPB) [54], *i.e.*, metal/solid electrolyte/oxygen:

$$\frac{1}{2} O_2 + V_O^{\bullet\bullet} = O_O^x + 2 h^\bullet \tag{18}$$

Several models have been proposed to correlate the electrode reaction rate with the electrode microstructure [55–59]. It has been shown that the electrochemical rate depends widely on the vacancy and electron hole concentrations in the solid electrolyte. Moreover, the assumption of an electrode reaction occurring at the Triple-Phase boundary appears unrealistic because it would involve too high ionic current densities. Consequently, it has been proposed that the oxygen reduction takes place on a reaction zone that expands from the TPB line over the electrolyte surface constituting a narrow ring around the metal particles. It has also been shown that the oxygen electrode reaction is characterized by a slight inward expansion [54]. This concept has been recently referred to improve the electrochemical performance of cathodes of SOFC by addition of an ionic conductor within the mixed ionic-electronic conductor. The improvement has been justified by the expansion of the TPB [60].

The results obtained in the present study could be explained within the framework of this model. The SR mechanism on a metal/insulating support catalyst, assuming a TPB at the metal/support interface can be schematized in Fig. 12a.

According to this model, the CH_x species formed on the metal particles have to diffuse towards the TPB interface where occur reactions (7), *i.e.* oxidation of CH_x by oxygen species of the CGO support and simultaneous partial reduction of Ce(IV), and (8), *i.e.* oxidation of Ce (III) by water vapour. XPS characterization demonstrated unambiguously the presence of Ir^{4+} and Ir^{3+} in the Ir particles. As schematized in Fig. 12b, we assume that the catalytic SR reaction takes place in a zone around each Ir particle that involved both the ceria support and iridium oxide (IrO_{2-x}). We can also assume that iridium ions diffuse to the CGO surface around the metallic particles.

The experimental results reinforce this interpretation:

- The size of the Ir particles does not increase noticeably in spite of high temperature experiments (usually high temperature favours the
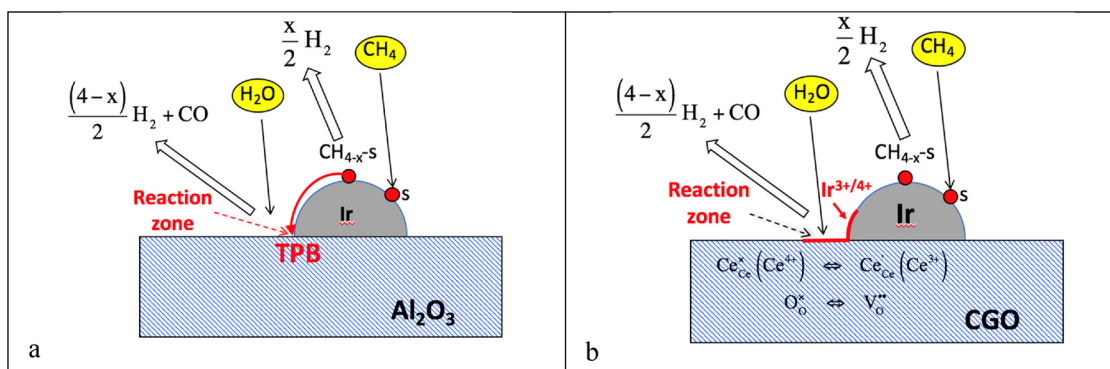
Fig. 12. a) Scheme of the mechanism of the SR of methane on a metal/insulating support catalyst b) Scheme of the mechanism of the SR of methane on a metal/MIEC support catalyst.

sintering of small particles to form large particles). We can assume that the reaction zone formed around the TPB anchors the particles and inhibit the size growth. Moreover, the chemical reaction between iridium ions and CGO reduces the size of the metallic particles.

- The slow activation of the catalyst (one day to obtain stabilized activity) could be explained by the formation of the reaction zone that involves mass transfer.

- As observed for oxygen electrode reaction, the expansion zone is characterized by a narrow ring around the Ir particle where the reactions take place without noticeable diffusion step.

- The expansion depends mainly on the nature of the support and mainly on its electrical and electrochemical properties. The expansion zone will be negligible on an insulating support such as Al_2O_3 or SiO_2, limited on a pure ionic conductor such as stabilized zirconia and larger on a mixed ionic-electronic conductor such as CGO. Note that the formation of a reaction zone around the metal catalyst on zirconia support appears more realistic than the hypothesis of zirconia reduction by methane [61–63].

- The expansion zone also depends on temperature. Consequently, the catalytic activity tends to a constant value, which increases with temperature.

- The high catalytic activity, taking into account the very low iridium content could be explained, considering that reactions (7) and (8) take place simultaneously on the reaction zone. It can be assumed that intermediate species can be formed with higher activity than molecules. This feature could also explain the inhibition of carbon formation on the catalyst.

5. Conclusions

Ir/CGO catalyst containing 0.1 wt% Ir was studied in the steam reforming of methane at 923 K under water deficient conditions (4.6:1 CH_4/H_2O ratio). Before catalytic testing, the catalyst was treated at 1173 K in pure inert gas (He) to feature the thermal step during the preparation of the cell. Although the conditions were thermodynamically favourable to the extensive deposition of carbon, very few amounts of carbon formed during the reaction, confirming the unique property of this catalyst over Ni catalysts to kinetically control and inhibit the formation of carbon. The CH_4 conversion rate was observed to gain one order of magnitude and stabilize over 16 h testing. This was shown to be related to structural and chemical modifications of the catalyst induced by the reaction mixture at 923 K. Upon activation in inert gas, Ir was dispersed on the CGO support as metallic nanoparticles of 4 nm in size. The methane activation, which is the rate determining step of the SR reaction, is thought to proceed at the surface of Ir nanoparticles and is not influenced by the CGO support. The role of the support would be to prevent extensive carbon deposition by easy reaction with mobile surface O species. Exposure to the reaction mixture at 923 K progressively induced the partial reoxidation of the iridium

phase into Ir^{3+}/Ir^{4+} species and the decrease of the mean particle size of the metallic particles to 1.7 nm. We propose that the activation of the Ir/CGO catalyst in the reaction mixture is due to the formation of nanometric reaction zones around Ir nanoparticles involving both mobile O species of the CGO support and oxidized Ir species in the catalytic reaction.

References

[1] X.-Y. Zhao, Q. Yao, S.-Q. Li, N.-S. Cai, Studies on the carbon reactions in the anode of deposited carbon fuel cells, J. Power Sources 185 (2008) 104–111.

[2] W. Wang, C. Su, Y. Wu, R. Ran, Z. Shao, Progress in solid oxide fuel cells with nickel-based anodes operating on methane and related fuels, Chem. Rev. 113 (2013) 8104–8151.

[3] C. Guerra, A. Lanzini, P. Leone, M. Santarelli, N.P. Brandon, Optimization of dry reforming of methane over Ni/YSZ anodes for solid oxide fuel cells, J. Power Sources 245 (2014) 154–163.

[4] Y.M. Park, H. Kim, An additional layer in an anode support for internal reforming of methane for solid oxide fuel cells, Int. J. Hydrogen Energy 39 (2014) 16513–16523.

[5] J. Laurencin, F. Lefebvre-Joud, G. Delette, Impact of cell design and operating conditions on the performances of SOFC fuelled with methane, J. Power Sources 177 (2008) 355–368.

[6] A. Thallam Thattai, L. van Biert, P.V. Aravind, On direct internal methane steam reforming kinetics in operating solid oxide fuel cells with nickel-ceria anodes, J. Power Sources 370 (2017) 71–86.

[7] E.P. Murray, T. Tsai, S.A. Barnett, A direct-methane fuel cell with a ceria-based anode, Nature 400 (1999) 649–651.

[8] O.A. Marina, M. Mogensen, High-temperature conversion of methane on a composite gadolinia-doped ceria–gold electrode, Appl. Catal. A Gen. 189 (1999) 117–126.

[9] M. Wisniewski, A. Boréave, P. Gélin, Catalytic CO_2 reforming of methane over Ir/$Ce_{0.9}Gd_{0.1}O_{2-x}$, Catal. Commun. 6 (2005) 596–600.

[10] B. Mosqueda, J. Toyir, A. Kaddouri, P. Gélin, Steam reforming of methane under water deficient conditions over gadolinium-doped ceria, Appl. Catal. B Environ. 88 (2009) 361–367.

[11] J. Toyir, P. Gélin, H. Belatel, A. Kaddouri, Ir/$Ce_{0.9}Gd_{0.1}O_{2-x}$ as a new potential anode component in solid oxide fuel cells integrating the concept of gradual internal reforming of methane, Catal. Today 157 (2010) 451–455.

[12] P. Vernoux, J. Guindet, M. Kleitz, Gradual internal methane reforming in intermediate-temperature solid-oxide fuel cells, J. Electrochem. Soc. 145 (1998) 3487–3492.

[13] S. Georges, G. Parrour, M. Henault, J. Fouletier, Gradual internal reforming of methane: a demonstration, Solid State Ionics 177 (2006) 2109–2112.

[14] S.D. Nobrega, F.C. Fonseca, P. Gélin, F.B. Noronha, S. Georges, M.C. Steil, Fuel-flex SOFC running on internal gradual reforming, ECS Trans. 57 (2013) 2885–2891.

[15] S.D. Nobrega, M.V. Galesco, K. Girona, D.Z. De Florio, M.C. Steil, S. Georges, F.C. Fonseca, Direct ethanol solid oxide fuel cell operating in gradual internal reforming, J. Power Sources 213 (2012) 156–159.

[16] S.D. Nobrega, F.C. Fonseca, P. Gélin, F.B. Noronha, S. Georges, M.C. Steil, Gradual

internal reforming of ethanol in solid oxide fuel cells, Energy Procedia 28 (2012) 28–36.

[17] S. Georges, N. Bailly, M.C. Steil, Y. Bultel, A. Hadjar, J.-P. Viricelle, M. Rieu, SOFC Long term operation in pure methane by gradual internal reforming, ECS Trans. 57 (2013) 3023–3030.

[18] K. Girona, S. Sailler, P. Gélin, N. Bailly, S. Georges, Y. Bultel, Modelling of gradual internal reforming process over Ni-YSZ SOFC anode with a catalytic layer, Can. J. Chem. Eng. 93 (2015) 285–296.

[19] J.P. Huijsmans, F.P. van Berkel, G. Christie, Intermediate temperature SOFC – a promise for the 21st century, J. Power Sources 71 (1998) 107–110.

[20] J.M. Ginsburg, J. Piña, T. El Solh, H.I. De Lasa, Coke formation over a nickel catalyst under methane dry reforming conditions: thermodynamic and kinetic models, Ind. Eng. Chem. Res. 44 (2005) 4846–4854.

[21] M.C. Annesini, V. Piemonte, L. Turchetti, Carbon formation in the steam reforming process: a thermodynamic analysis based on the elemental composition, Chem. Eng. Trans. 11 (2007) 21–26.

[22] S.D. Angeli, G. Monteleone, A. Giaconia, A.A. Lemonidou, State-of-the-art catalysts for CH_4 steam reforming at low temperature, Int. J. Hydrogen Energy 39 (2014) 1979–1997.

[23] G. Postole, T.S. Nguyen, M. Aouine, P. Gélin, L. Cardenas, L. Piccolo, Efficient hydrogen production from methane over iridium-doped ceria catalysts synthesized by solution combustion, Appl. Catal. B Environ. 166–167 (2015) 580–591.

[24] E. Ramírez-Cabrera, A. Atkinson, D. Chadwick, Catalytic steam reforming of methane over $Ce0.9Gd_{0.1}O_{2-x}$, Appl. Catal. B Environ. 47 (2004) 127–131.

[25] X. Wang, R.J. Gorte, A study of steam reforming of hydrocarbon fuels on Pd/ceria, Appl. Catal. A Gen. 224 (2002) 209–218.

[26] R. Craciun, B. Shereck, R.J. Gorte, Kinetic studies of methane steam reforming on ceria-supported Pd, Catal. Letters 51 (1998) 149–153.

[27] M.H. Halabi, M.H.J.M. De Croo, J. Van Der Schaaf, P.D. Cobden, J.C. Schouten, Low temperature catalytic methane steam reforming over ceria–zirconia supported rhodium, Appl. Catal. A Gen. 389 (2010) 68–79.

[28] E. Ramírez-Cabrera, A. Atkinson, D. Chadwick, Reactivity of ceria, Gd- and Nd-doped ceria to methane, Appl. Catal. B Environ. 36 (2002) 193–206.

[29] J. Wei, E. Iglesia, Isotopic and kinetic assessment of the mechanism of methane reforming and decomposition reactions on supported iridium catalysts, Phys. Chem. Chem. Phys. 6 (2004) 3754–3759.

[30] G. Postole, K. Girona, J. Toyir, A. Kaddouri, P. Gélin, Catalytic steam methane reforming Over $Ir/Ce_{0.9}Gd_{0.1}O_{2-x}$: resistance to coke formation and sulfur poisoning, Fuel Cells 12 (2012) 275–287.

[31] V. Pfeifer, T.E. Jones, J.J. Velasco Vélez, C. Massué, R. Arrig, D. Teschner, F. Girgsdies, M. Scherzer, M.T. Greiner, J. Allan, M. Hashagen, G. Weinberg, S. Piccinin, M. Hävecker, A. Knop-Gericke, R. Schlögl, The electronic structure of iridium and its oxides, Surf. Interface Anal. 48 (2016) 261–273.

[32] D.F. Abbott, D. Lebedev, K. Waltar, M. Povia, M. Nachtegaal, E. Fabbri, C. Copéret, T.J. Schmidt, Iridium oxide for the oxygen evolution reaction: correlation between particle size, morphology, and the surface hydroxo layer from operando XAS, Chem. Mater. 28 (2016) 6591–6604.

[33] J. Jellinek, P.H. Acioli, Magnesium clusters: structural and electronic properties and the size-induced nonmetal-to-metal transition, J. Phys. Chem. A 106 (2002) 10919–10925.

[34] M. Bianchi, D. Cassese, A. Cavallin, R. Comin, F. Orland, L. Postregna, E. Golfetto, S. Lizzit, A. Baraldi, Surface core level shifts of clean and oxygen covered Ir(111), New J. Phys. 11 (2009) 63002.

[35] E.H.P. Cordfunke, The enthalpy of formation of IrO_2 and thermodynamic functions, Thermochim. Acta 50 (1981) 177–185.

[36] J.L. Rousset, F.J. Cadete Santos Aires, B.R. Sekhar, P. Mélinon, B. Prevel, M. Pellarin, Comparative x-ray photoemission spectroscopy study of Au, Ni, and AuNi clusters produced by laser vaporization of bulk metals, J. Phys. Chem. B 104 (2000) 5430–5435.

[37] P. Scanlon, R.A.M. Bink, F.P.F. van Berkel, G.M. Christie, L.J. van IJzendoorn, H.H. Brongersma, R.G. van Welzenis, Surface composition of ceramic CeGd-oxide, Solid State Ionics 112 (1998) 123–130.

[38] X. Aparicio-Anglès, A. Roldan, N.H. De Leeuw, Gadolinium-vacancy clusters in the (111) surface of gadolinium-doped ceria: a density functional theory study, Chem. Mater. 27 (2015) 7910–7917.

[39] H. Borchert, Y.V. Frolova, V.V. Kaichev, I.P. Prosvirin, G.M. Alikina, A.I. Lukashevich, V.I. Zaikovskii, E.M. Moroz, S.N. Trukhan, V.P. Ivanov, E.A. Paukshtis, V.I. Bukhtiyarov, V.A. Sadykov, Electronic and chemical properties of nanostructured cerium dioxide doped with praseodymium, J. Phys. Chem. B 109 (2005) 5728–5738.

[40] M. Florea, G. Postole, F. Matei-Rutkovska, A. Urda, F. Neatu, L. Massin, P. Gelin, Influence of Gd and Pr doping on the properties of ceria: texture, structure, redox behaviour and reactivity in CH_4/H_2O reactions in the presence of H_2S, Catal. Sci. Technol. 8 (2018) 1333–1348.

[41] H. Sohn, G. Celik, S. Gunduz, D. Dogu, S. Zhang, J. Shan, F.F. Tao, U.S. Ozkan, Oxygen mobility in pre-reduced nano- and macro-ceria with Co loading: an AP-XPS, in-situ DRIFTS and TPR study, Catal. Lett. 147 (2017) 2863–2876.

[42] J.M. López, A.L. Gilbank, T. García, B. Solsona, S. Agouram, L. Torrente-Murciano, The prevalence of surface oxygen vacancies over the mobility of bulk oxygen in nanostructured ceria for the total toluene oxidation, Appl. Catal. B: Environ. 174-175 (2015) 403–412.

[43] S.K. Cheah, V.P. Bernardet, A.A. Franco, O. Lemaire, P. Gélin, Study of CO and hydrogen interactions on carbon-supported Pt nanoparticles by quadrupole mass spectrometry and operando diffuse reflectance FTIR spectroscopy, J. Phys. Chem. C 117 (2013) 22756–22767.

[44] M.A. Vannice, Kinetics of Catalytic Reactions, Springer, US, New York, 2005.

[45] J. Wei, E. Iglesia, Mechanism and site requirements for activation and chemical conversion of methane on supported Pt clusters and turnover rate comparisons among noble metals, J. Phys. Chem. B 108 (2004) 4094–4103.

[46] J. Wei, E. Iglesia, Structural and mechanistic requirements for methane activation and chemical conversion on supported iridium clusters, Angew. Chem. Int. Ed. 43 (2004) 3685–3688.

[47] R.A. Van Santen, Complementary structure sensitive and insensitive catalytic relationships, Acc. Chem. Res. 42 (2009) 57–66.

[48] M.F. Mark, W.F. Maier, CO_2-reforming of methane on supported Rh and Ir catalysts, J. Catal. 164 (1996) 122–130.

[49] A. Bruix, J. Rodriguez, P.J. Ramirez, S. Senanayabe, J. Evans, J.B. Park, D. Stacchiola, P. Liu, J. Hrbek, F. Illas, A new type of strong metal-support interaction and the productin of H_2 through the transformation of Water on Pt/CeO_2(111) and Pt/CeO_2/TiO_2(110) catalysts, J. Am. Chem. Soc. 134 (2012) 8968–8974.

[50] Y. Lykhach, S.M. Kozlov, T. Skála, A. Tovt, V. Stetsovych, N. Tsud, F. Dvořák, V. Johánek, A. Neitzel, J. Mysliveček, S. Fabris, V. Matolín, K.M. Neyman, J. Libuda, Counting electrons on supported nanoparticles, Nat. Mater. 15 (2016) 284–288.

[51] M. Flytzani-Stephanopoulos, B.C. Gates, Atomically dispersed supported metal catalysts, Annu. Rev. Chem. Biomol. Eng. 3 (2012) 545–574.

[52] Z. Liu, D.C. Grinter, P.G. Lustemberg, T.-D. Nguyen-Phan, Y. Zhou, S. Luo, I. Waluyo, E.J. Crumlin, D.J. Stacchiola, J. Zhou, J. Carrasco, H.F. Busnengo, M.V. Ganduglia-Pirovano, S.D. Senanayake, J.A. Rodriguez, Dry reforming of methane on a highly-active Ni-CeO_2 catalyst: effects of metal-support interactions on C–H bond breaking, Angew. Chem. Intern. Ed. 55 (2016) 7455–7459.

[53] A. Bruix, Y. Lykhach, I. Matolínová, A. Neitzel, T. Skála, N. Tsud, M. Vorokhta, V. Stetsovych, K. Ševčíková, J. Mysliveček, R. Fiala, M. Václavů, K.C. Prince, S. Bruyère, V. Potin, F. Illas, V. Matolín, J. Libuda, K.M. Neyman, Maximum noble-metal efficiency in catalytic materials: atomically dispersed surface platinum, Angew. Chem. Int. Ed. Engl. 53 (2014) 10525–10530.

[54] R. Jiménez, T. Kloidt, M. Kleitz, Reaction-zone expansions and mechanism of the O_2, Ag/Yttria-stabilized zirconia electrode reaction, J. Electrochem. Soc. 144 (1997) 582–585.

[55] J. Misuzaki, H. Tagawa, K. Tsuneyoshi, A. Sawata, Reaction kinetics and microstructure of the solid oxide fuel cells air electrode La0.6Ca$_{0.4}$MnO$_3$ / YSZ, J. Electrochem. Soc. 138 (1991) 1867–1873.

[56] O.J. Velle, T. Norby, P. Kofstad, The electrode system O_2/Pt//ZrO_2: $8Y_2O_3$ investigated by impedance spectroscopy, Solid State Ionics 47 (1991) 161–167.

[57] T. Kenjo, Y. Yamakoshi, K. Wada, An estimation of the electrode-electrolyte contact Area by linear sweep voltammetry in Pt / ZrO_2 oxygen electrodes, J. Electrochem. Soc. 140 (1993) 2151–2157.

[58] M. Kleitz, T. Kloid, L. Dessemond, Conventional oxygen electrode reaction: facts and models, in high temperature electrochemical behaviour of fast ion and mixed conductors, in: F.W. Poulsen, J.J. Bentzen, T. Jacobsen, E. Skou, M.J.L. Østergaard (Eds.), Proc. 14th Risø Int. Symp. on Materials Sci. Risø National Lab. Publ., Roskilde, Denmark, 1993, pp. 89–116.

[59] M. Kleitz, L. Dessemond, T. Kloidt, M.C. Steil, Space expansions of the regular oxygen electrode reaction on YSZ - II. Silver electrodes, in solid oxide fuel cells IV, in: M. Dokiya, O. Yamamoto, H. Tagawa, S.C. Singhal (Eds.), PV 95-1, The Electrochem. Soc. Proc. Series, 1995, pp. 527–536.

[60] M. Guan, W. Sun, R. Ren, Q. Fan, J. Qiao, Z. Wang, D. Rooney, J. Feng, K. Sun, Improved electrochemical performance of Sr$_2$Fe1.5Mo$_{0.4}$Nb$_{0.1}$Sm$_{0.2}$Ce$_{0.8}$O$_{2-\delta}$ composite cathodes by a one-pot method for intermediate temperature solid oxide fuel cells, Int. J. Hydrogen Energy 41 (2016) 3052–3061.

[61] S.M. Stagg, E. Romeo, C. Padro, D.E. Resasco, Effect of promotion with Sn on supported Pt catalysts for CO_2 reforming of CH_4, J. Catal. 178 (1998) 137–145.

[62] S.M. Stagg-Williams, F.B. Noronha, G. Fendley, D.E. Resasco, CO_2 reforming of CH_4 over Pt/ZrO_2 catalysts promoted with La and Ce oxides, J. Catal. 194 (2000) 240–249.

[63] S. Sharma, S. Hilaire, J.M. Vohs, R.J. Gorte, H.-W. Jen, Evidence for oxidation of ceria by CO_2, J. Catal. 190 (2000) 199–204.